ARTICLE   OPEN

Check for updates

Point-defect-driven flattened polar phonon bands in fluorite ferroelectrics

Pu Ai[1,6], Fengjun Yan [1,6], Wen Dong[1 ✉], Shi Liu [2], Junlei Zhao [3], Kan-Hao Xue [1], Syed Ul Hasnain Bakhtiar[1], Yilong Liu[1], Qi Ma[1], Ling Miao[3], Mengyuan Hua[4], Guangzu Zhang[1], Shenglin Jiang[1], Wei Luo[1] and Qiuyun Fu[1,5 ✉]

The scale-free ferroelectric polarization of fluorite MO_2 (M = Hf, Zr) due to flat polar phonon bands are promising for nonvolatile memories. Defects are also widely introduced to improve the emergent ferroelectricity. However, their roles are still not fully understood at the atomic-level. Here, we report a significant effect of point-defect-driven flattening of polar phonon bands with more polar modes and polarization contribution in doped MO_2. The polar phonon bands in La-doped MO_2 (M = Hf, Zr) can be significantly flattened, compared with pure ones. However, the lower energy barrier with larger polarization of V_O-only doped MO_2 compared with La-doped cases suggest that V_O and local lattice distortion should be balanced for high-performance fluorite ferroelectricity. The work is believed to bridge the relation between point defects and the generally enhanced induced ferroelectricity in fluorite ferroelectrics at the atomic-level and inspire their further property optimization via defect-engineering.

INTRODUCTION

Ferroelectric materials are technologically important and promising for nonvolatile memories owning to their fast switchable polarization and relatively low energy consumption[1,2]. However, the size effect in conventional perovskite ferroelectrics has suppressed their further down-scaling when silicon semiconductor process is coming to a sub-ten nanometer era[3]. Recently, the discovery of robust scale-free ferroelectricity in MO_2 (M = Hf, Zr) based fluorite thin films sheds light on next-generation ferroelectric-based nano-electronic memories[4–6].

The fluorite-based ferroelectrics are distinct from conventional perovskite ferroelectrics because of their complex origin of ferroelectricity in relation to metastable ferroelectric phase and defects. Both HfO_2 and ZrO_2 show stable monoclinic phase in their bulk form. While, some high-temperature or high-pressure phases, such as cubic and tetragonal, can be stabilized and exist metastably at room temperature in the fluorite structure via doping and nano-structuring[7]. However, none of the above structures are reported to be polar until the discovery of polar orthorhombic phase in Mg-doped ZrO_2 at cryogenic temperature[8]. Since then, tremendous MO_2 (M = Hf, Zr) based thin films doped with different dopants were reported to show ferroelectric orthorhombic phase on either Si or oxide substrates as well as with noble metal or metal nitride electrode[9]. Moreover, Y-doped HfO_2 single crystal and epitaxial rhombohedral $Hf_{0.5}Zr_{0.5}O_2$ thin film ferroelectrics prepared by state-of-the-art methods have further advanced the understanding of the polymorphic nature and phase control of HfO_2- and ZrO_2-based fluorite oxides[10,11].

Compared with pure HfO_2 and ZrO_2 that have limited or nearly no polarization[6,12,13], dramatically enhanced ferroelectricity can be induced in doped cases generally due to the stabilization of polar orthorhombic phase in either ultrathin film or small grains from an average structure point of view[9,10,14–17]. It is widely accepted that defect plays an important role in not only the induced/enhanced ferroelectricity but also the fatigue and bipolar-cycling performance[18]. Recently, it is also suggested that a small rhombohedra distortion in the polar orthorhombic phase by structural defects can effectively improve the ferroelectricity[14]. However, there is still no clear point to bridge the relation between point defects and ferroelectricity at the atomic level in fluorite ferroelectrics. Lee et al.[4] recently pointed out that flat polar phonon bands with localization of electric dipoles lead to the scale-free ferroelectricity in HfO_2, which as well explains the generally high coercive field and makes it distinct from the conventional ferroelectrics with spread dipoles. This atomic level understanding of the ferroelectricity indicates that the mechanism of the defect-enhanced ferroelectricity may be also significantly different from that of the conventional ferroelectrics where defects either negatively act as leaky center or positively improve ferroelectric polarization via correlation between defect-dipoles and intrinsic polarization[19–25]. Actually, even in non-ferroelectric metal oxides, defect-dipoles with relatively large dipole moment can lead to high-performance colossal dielectric permittivity (>10000) behavior[26–28], collective nonlinear electric polarization in either bulk ceramics or ultrathin films[29,30]. In this consideration, we believe that it is hard to neglect the effect of defect-dipole polarization on the macroscopic polarization of fluorite-based ferroelectric system where dominant monoclinic phase and slight amount of metastable polar orthorhombic phase coexists. Therefore, how the defect affects the ferroelectricity and how it correlates with its nearby environment at the atomic level remains an important question.

Here, by using the first principal density functional theory (DFT) calculation, similar as that of the HfO_2 system, we confirmed that the flat polar phonon bands in orthorhombic-phase (o-phase) ZrO_2 with localized electric dipoles to give rise to the scale-free
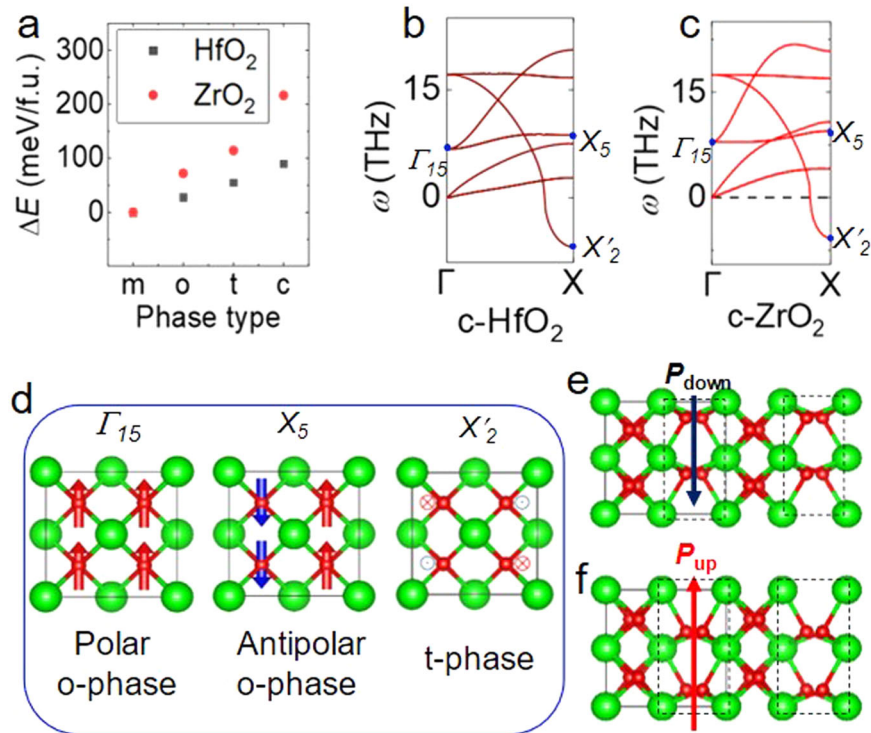
Fig. 1 The origin of the ferroelectricity in fluorite MO_2 (M = Hf, Zr). a Calculated difference of total energy ΔE for crystal m-phase, o-phase, t-phase, and c-phase for fluorite MO_2 (M = Hf, Zr). $\Delta E = E_{\text{other-phase}} - E_{\text{m-phase}}$ (in unit meV per formular unit MO_2, meV/f.u.), green and red spheres indicate Hf/Zr and O, respectively. **b, c** Phonon dispersion spectra of c-HfO$_2$ and c-ZrO$_2$ and their symmetry-lowering steps. The blue dots labeled Γ_{15}, X_5, and X'_2 indicate the primary instability modes in Γ and X wave vectors. **d** The phonon modes Γ_{15}, X_5, and X'_2 correspond to transformations to polar-, antipolar-, and t-phase, respectively. The Γ_{15} and X_5 modes condense in phase with equal magnitude to generate an orthorhombic structure that is periodically sandwiched between dead spacer layers. The arrows denote the polarization due to the displacement of oxygen atoms. **e, f** The above two inset images show the orthorhombic structures with polarization up and polarization down respectively (indicated by the dashed rectangular region) and periodically sandwiched between spacer layer. The green spheres indicate Hf/Zr, while the red spheres indicate oxygen.

ferroelectricity. In order to figure out the bridge between defects and ferroelectricity at the atomic level, by taking oxygen vacancy-only (V_O -only) La-doped MO_2 (M = Hf, Zr) as examples, we report a dramatically enhanced flattening of polar phonon bands. The polar phonon bands in La-MO_2 (M = Hf, Zr) becomes significantly flattened at an optimal doping level, compared with pure ones. The dramatically flattened polar phonon bands fundamentally enhances the polar states in orthorhombic phase, which is consistent with the enhanced ferroelectricity in La-doped HfO$_2$ and also imply a similarly enhanced ferroelectricity in doped ZrO$_2$. We further found that point-defect-dipoles polarize surrounding host ions, which forms partially localized electric dipoles and partially diffuse the sharp zero-width domain walls. The localized electric dipoles and spread dipoles together lead to an enhanced polar state should provide an atomic-level insight for the origin of ferroelectricity in doped fluorite ferroelectrics. However, the lower energy barrier with larger polarization of V_O-only doped MO_2 suggest that V_O and local lattice distortion should be considered to further optimize their ferroelectric properties. This research is believed to provide a missing link between defects and induced ferroelectricity in fluorite ferroelectrics, which would inspire their property-optimization.

RESULTS AND DISCUSSION

Transformation of phonon band structure in pure fluorite MO$_2$ (M = Hf and Zr)

Both HfO$_2$ and ZrO$_2$ mainly have three kinds of crystal phases[31], including monoclinic phase (m-phase, space group $P2_1/c$) at room

temperature, tetragonal phase (t-phase, space group $P4_2/nmc$) and cubic phase (c-phase, space group $Fm3m$) at high temperature[32]. Orthorhombic phase (o-phase, space group $Pca2_1$) was discovered under extreme conditions (high pressure and temperature)[33,34]. To determine the origin of polar orthorhombic phase in fluorite MO_2 (M = Hf and Zr), we calculated the free energies of the four phases after structural relaxation. Figure 1a show the free energy difference ΔE between m-phase and other phases by $\Delta E = E_{\text{other-phase}} - E_{\text{m-phase}}$ (in unit meV/f.u.). The lowest energy phase (m-phase), which exists at room temperature, is the most stable phase for MO_2 (M = Hf, Zr). On the contrary, t-phase and c-phase just exist at very high temperature. The smaller ΔE of the o-phase than t-phase suggests more metastability of o-phase. It should be noted that among the four phases, only o-phase is polar.

To analyze the symmetry-lowering process, we calculated the phonon spectra of c-phase HfO$_2$ and ZrO$_2$ (c-HfO$_2$ and c-ZrO$_2$) as shown in Fig. 1b, c. The blue dots labeled Γ_{15}, X_5, and X'_2 indicate the primary modes in Γ and X wave vectors where the first two respectively correspond to polar and antipolar phonon modes that combine in-phase with equal magnitude to generate an orthorhombic structure that is ferroelectrically active and periodically sandwiched between dead spacer layers. The structurally instable X'_2 modes at $\omega = -6.80$ THz in HfO$_2$ and $\omega = -5.75$ THz in ZrO$_2$ involve the antiparallel x-axis displacements of neighboring oxygen atoms in the yz plane, which transforms c-phase to t-phase through the condensation of X'_2 mode with zero net polarization (Fig. 1d). This fact significantly suggests the main contribution from anion oxygen displacement rather than cation in ZrO$_2$ compared with conventional perovskite ferroelectric where ferroelectricity is originated from displacement of cations.
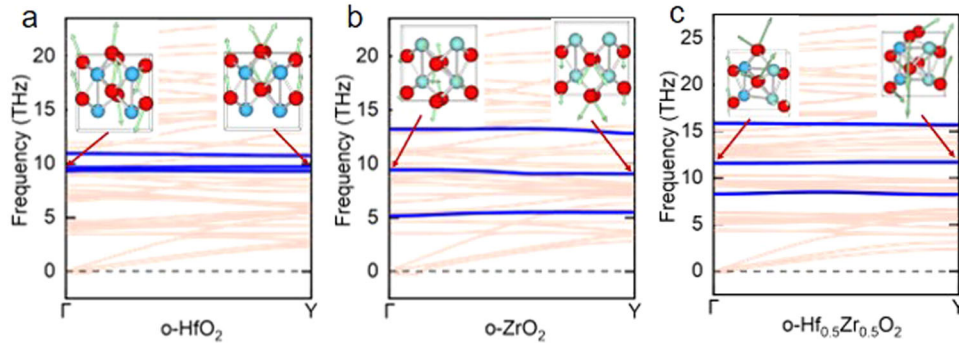
Fig. 2 Flat polar phonon bands in o-phase MO_2 ($M =$ Hf, Zr). a Phonon spectra of o-HfO$_2$ where the flat polar phonon eigenmodes from Γ (~9.66 THz) and Y (~9.71 THz) wave vectors were indicated, respectively. **b** Phonon spectra of o-ZrO$_2$ where the flat polar phonon eigenmodes from Γ (~9.07 THz) and Y (~9.42 THz) wave vectors were indicated, respectively. **c** Phonon spectra of o-Hf$_{0.5}$Zr$_{0.5}$O$_2$ where the flat polar phonon eigenmodes from Γ (~11.58 THz) and Y (~ 11.70 THz) wave vectors were indicated, respectively. The blue lines indicate the flat polar phonon band where the frequency difference $\Delta\omega$ between Γ to Y points is within 0.5 THz. The red spheres and aqua green spheres indicate oxygen and host cation, respectively.

This result suggests that the symmetry of the c-phase is lowered to o-phase and can generate mixed antiferroelectric and ferroelectric states in both HfO$_2$ and ZrO$_2$, which is consistent with the symmetry lowering process reported in HfO$_2$[4].

The transition energy barrier between the two ferroelectric configurations (P_{down} and P_{up}) via spacer layer has been calculated by nudged elastic band (NEB) method[35] as shown in Fig. 1e. The flatness of phonon bands demonstrates nearly zero group velocity and domain walls propagate slowly by hopping the large energy barrier (1.35 eV in HfO$_2$ and 1.16 eV in ZrO$_2$) as shown in Fig. 1e, which is two orders of magnitude higher compared with the energy barrier (0.02 eV) of conventional perovskite ferroelectrics with diffused domain walls[4]. The spontaneous polarization (P_s) in o-phase MO_2 ($M =$ Hf, Zr) was calculated by Berry phase and NEB method between polarization up and down o-phase. The energy-polarization curve (E-P) conforms to the double-well potential of Landau-Ginsberg-Devonshire theory. The P_S values of HfO$_2$ is 70.00 μC·cm^-2, which is close to other theoretical calculations[35]. Compared with HfO$_2$, though o-ZrO$_2$ shows a slightly lower P_S value of 64.70 μC·cm^-2, its but much lower energy barrier indicates a lower coercive field compared with HfO$_2$.

We further uncovered the phonon band structure of the o-phase with polar flat phonon band structures highlighted in blue color as shown in Fig. 2. Both o-HfO$_2$ and o-ZrO$_2$, and o-Hf$_{0.5}$Zr$_{0.5}$O$_2$ show a small negative frequency at Γ point, which should be partially due to the inaccuracy of the calculation and partially due to that o-phase is metastable since o-phase only exists under some extreme conditions, including thin films down to nanometer scale, high temperature and pressure (more detail see Supplementary Figs. 1–3). It should be noted that there is an obvious signature of flat polar phonon bands indicated by the two blue lines in Fig. 2a, b compared with c-phase cases (Fig. 1b, c). There are several distinct flat polar phonon bands (blue line) from Γ to Y wave vectors by the partially shown vibration modes with obvious oxygen displacement where the superposition of the two bands at Γ and Y gives rise to the localized electric dipoles similarly as shown in Fig. 1d. Here, by taking the bands with frequency difference $\Delta\omega$ between Γ to Y wave vectors within 0.5 THz as flat phonon bands, nearly ~29.7%, ~27.8%, and ~35.1% of the phonon bands are flat among the band structures in HfO$_2$, ZrO$_2$, and Hf$_{0.5}$Zr$_{0.5}$O$_2$, respectively. The substantial amount of flat polar phonon bands indicates an increased possibility of the coherent polar modes, which should be intrinsically responsible for its zero-width domain wall and scale-free ferroelectricity[17,35]. These results suggest that this kind of flat polar phonon behavior is a universal phenomenon in fluorite-based oxide.

Defective and stressed fluorite MO_2 ($M =$ Hf and Zr)

As we mentioned before, for pure fluorite MO_2 ($M =$ Zr and Hf), it is either difficult to see obvious ferroelectricity or the ferroelectricity is relatively weaker compared with doped cases. As shown in Fig. 3a, the reported highest values of remnant polarization (P_r) in the rare-earth doped cases or solid solution of Hf$_{0.5}$Zr$_{0.5}$O$_2$ are generally at least two times larger than that of the pure ones followed by a stabilized o-phase[6,14,36–44]. Though ZrO$_2$ thin film has been reported to have P_r as high as over 50 μC·cm^-2 after annealing in N$_2$ atmosphere, but the high leaky current makes it hardly to neglect the substantial contribution of defects like oxygen vacancy in addition to texture growth[14,37]. Therefore, the polar o-phase in MO_2 ($M =$ Zr, and Hf) can be stabilized by V_O and additional dopants, such as La, Si, Al, Y, consequently, inducing or enhancing ferroelectricity[6,10,39]. Both Hf$_{0.5}$Zr$_{0.5}$O$_2$ and ZrO$_2$ show stable o-phase and enhanced ferroelectricity in atomically thin films deposited by ALD on Si substrate[5,6]. To understand the effect of point-defects on the ferroelectricity in fluorite binary oxides, it is necessary and important to investigate the flat polar phonon bands in the doped cases.

In this paper, we mainly focus on La-doped MO_2, which exhibits relatively high remnant polarization[15]. As the La concentration increases, the energy difference ΔE of each formula unit between o-phase and m-phase decreases gradually, indicating an enhanced stabilization of o-phase (Supplementary Fig. 4a). This is consistent with previous studies that a suitable concentration of dopant enhances the stability of ferroelectric o-phase. We calculated the phonon spectra of La$_x$M$_{1-x}$O$_{2-\delta}$ ($x =$ 6.25%-50%, $M =$ Hf and Zr), in which oxygen vacancies were introduced for charge neutrality. The coercive field above mega-volt (MV) level in ZrO$_2$ and HfO$_2$-based ferroelectric system should be large enough to manipulate the modes below 25 THz compared with that below 10 THz in conventional perovskite ferroelectric with only kV level coercive field (Supplementary Fig. 4b).

In order to more intuitively distinguish the degree of dispersion under different doping concentrations, $\Delta\omega$ of each phonon line was calculated (Supplementary Figs. 5 and 6). We set $\Delta\omega < 0.5$ THz as flat phonon band and calculated the total number of flat phonon bands in MO_2 ($M =$ Hf, Zr). Since the main ionic displacement is from oxygen and there is no obvious cation displacement, we will mainly consider the modes associated with oxygen displacement to contribute to the ferroelectricity in doped fluorite o-MO_2. To our surprise, all the La-doped MO_2 systems show significant flattened phonon band structures (more details see Supplementary Figs. 5 and 6). We have calculated supercells with sizes of $1 \times 1 \times 1$, $1 \times 2 \times 1$, and $2 \times 2 \times 1$ for comparisons. The
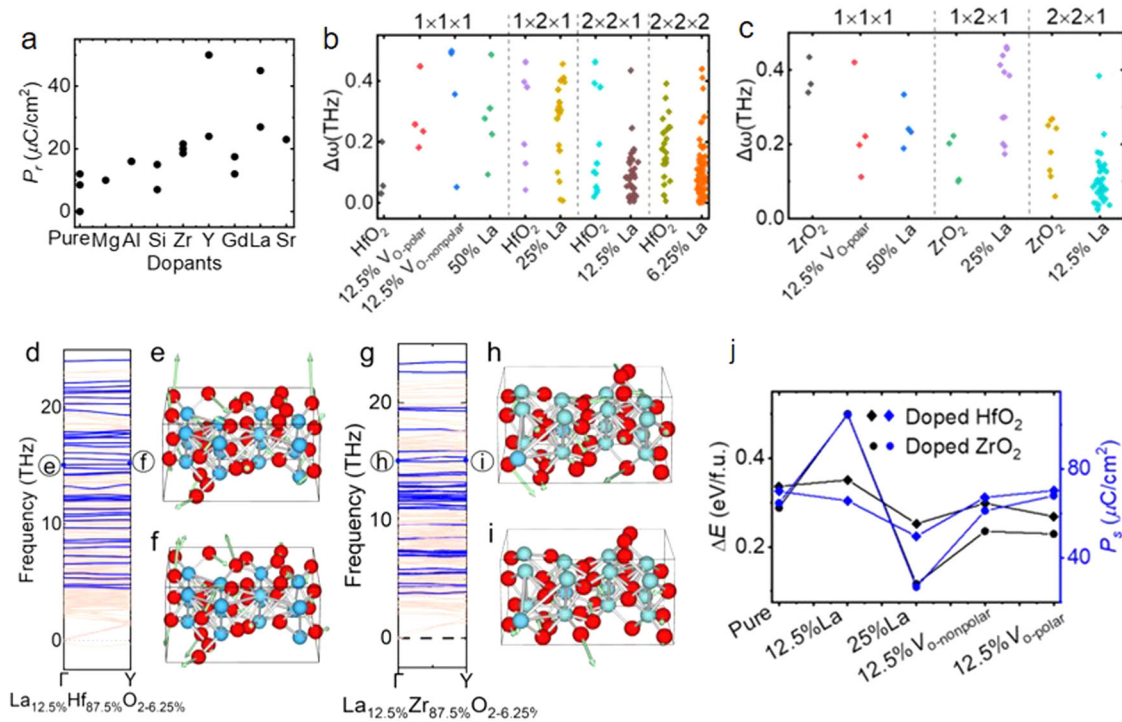
Fig. 3 Point-defect-induced flattening of phonon band structures in La-doped fluorite MO_2 (M = Hf, Zr). a Mapping of reported typical maximum remnant polarization values in pure and doped fluorite-based metal oxides MO_2 (M = Zr, and Hf) with different dopants[6,14,36–44]. **b**, **c** Comparison of the absolute values of the frequencies ($\Delta\omega < 0.5$ THz) of the polar bands from Γ to Y wave vectors for pristine and the doped cases with the same size supercells. **d** Phonon spectra of $La_{12.5\%}Hf_{87.5\%}O_{2-6.25\%}$ where the flat polar phonon modes from Γ (~15.08 THz) and Y (~15.10 THz) wave vectors indicated by **e** and **f**, respectively. **g** Phonon spectra of $La_{12.5\%}Zr_{87.5\%}O_{2-6.25\%}$ where the flat polar phonon modes from Γ (at 15.02 THz) and Y (at 15.05 THz) wave vectors at ~15.1 THz were indicated by **h** and **i**, respectively. Vo-nonpolar and Vo-polar mean the site of V_O at nonpolar region (spacer layer) and polar region (ferroelectric layer), respectively. **j** Evolution of energy barrier ΔE and spontaneous polarization (P_S) values in doped MO_2 (M = Hf, Zr).

supercell size of the $1 \times 1 \times 1$ is the same as that of the V_O-only-doped cases, while $1 \times 2 \times 1$ supercell is the same as that of the 25% La-doped HfO_2, $2 \times 2 \times 1$ supercell is the same as that of the 12.5% La-doped HfO_2, $2 \times 2 \times 2$ supercell is the same as that of the 6.25% La-doped HfO_2. These are similar as the cases in ZrO_2. As shown in Fig. 3b, the distribution frequency of the flat phonon bands ($\Delta\omega < 0.5$ THz) shows no obvious difference between pure o-HfO_2, V_O-only doped cases and 50% La doped case (more details see Supplementary Fig. 7). However, more modes become flat for La doped HfO_2 in the doping range of 6.25% to 25%. Figure 3c shows similar significantly flattened bands were observed in 12.5% and 25% La-doped ZrO_2 compared with that of the pure o-ZrO_2, V_O-only doped cases and 50% La-doped case (Supplementary Fig. 8). With this in mind, the dramatically flattened phonon bands would suggest a quasi-phonon-glass behavior and much lower thermal conductivity in specific direction[45,46]. Here, Vo at both polar layer (Vo-nonpolar) and nonpolar layer (Vo-nonpolar) are considered for the Vo-only doped case. Thus, it may also be expected to induce a giant thermal rectification effect to cater for the thermal dissipation in ferroelectric MO_2 based integrated circuits. This result is expected to extend the research of doping-induced thermal rectifying effect and would leads to potential applications for thermal rectifying materials and devices. These results suggest that V_O is helpful to transform nonpolar phase to polar phase and stabilize the o-phase, which is somehow consistent with the reversible oxygen vacancy related phase transition and ferroelectricity in hafnia-based ferroelectric devices[47–49]. The much of flat polar phonon bands with La-V_O defect pairs compared with V_O-only doped case suggests that the synergistic effect of defect-complex on the flattening of the polar phonon bands.

To confirm the polarization contribution of flat polar phonon modes, we calculated their corresponding lattice vibration modes that show net polarization after the condensation of modes from Γ to Y wave vectors. We mainly present two typical vibration modes for each spectrum by taking the 12.5% La-doped MO_2 (M = Hf, Zr) as examples where blue lines indicate the flat polar phonon bands (Fig. 3d). There is no obvious polar phonon band in the non-flat ones, which means that the main polarization contribution is from flat polar phonon bands. The selected typical flat polar phonon modes (blue dots) point to their lattice vibration modes. It is obvious that the two flat polar phonon modes at Γ and Y wave vectors not always condense in-phase with equal magnitude to generate an orthorhombic structure that is periodically sandwiched between spacer layers, leading to a net polarization rather than an antipolar behavior like that shown in Fig. 1d–f. In o-MO_2 (M = Hf, Zr). The antipolar spacer layers lead to a sharp/zero-width domain walls. While in doped HfO_2, such as $La_{12.5\%}Hf_{87.5\%}O_{2-6.25\%}$, the two typical flat polar phonon modes at Γ (~15.08 THz) (Fig. 3e) and Y (~15.10 THz) (Fig. 3f) points visibly not tend to condense in-phase with equal magnitude to generate a periodic antipolar/polar structure. Similar spread dipoles were also observed in doped ZrO_2, such as $La_{12.5\%}Zr_{87.5\%}O_{2-6.25\%}$ with the two typical flat polar phonon modes at Γ (~15.02 THz) (Fig. 3h) and Y (~15.05 THz) (Fig. 3i). Therefore, doping engineering would easily lead to spread dipoles and partially diffuse domain walls compared with pure ones with fully localized dipoles and zero-width domain walls. We also similarly confirmed the partially diffused domain walls by analyzing the flat polar phonon modes in La-doped MO_2 with other doping levels (Supplementary Figs. 5 and 6 and Table 1–2).
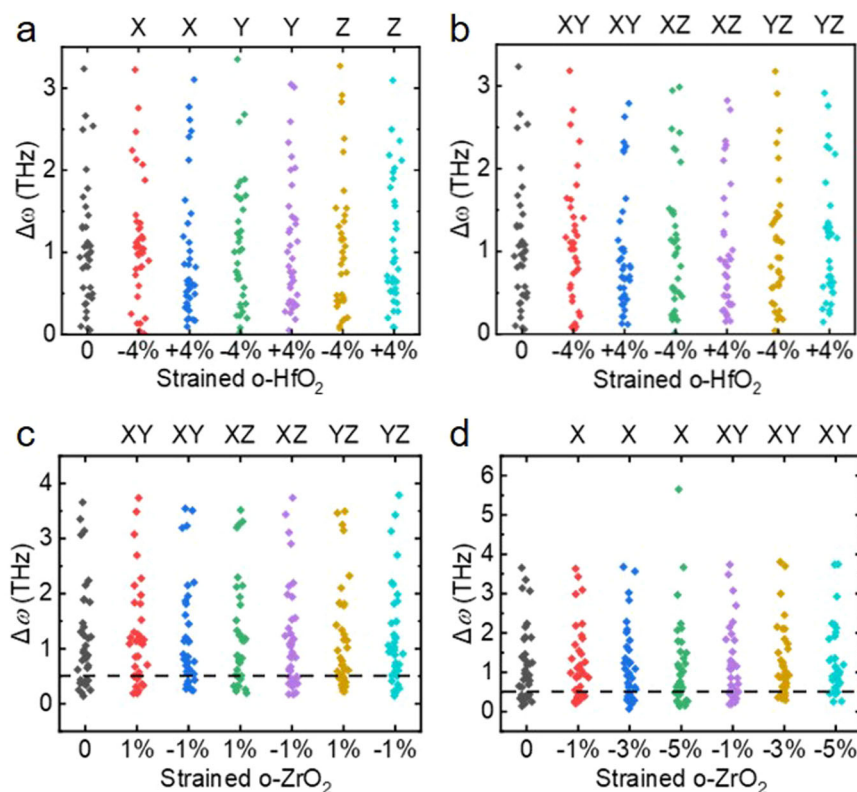
Fig. 4 Effect of strain on the phonon band structure of the fluorite o-MO_2 (M = Hf, Zr). a–d Comparison of the absolute values of the frequencies ($\Delta\omega$ < 0.5 THz) of the polar bands from Γ to Y wave vectors for pristine and the doped cases with the same size supercells in pure o-phase HfO$_2$ and ZrO$_2$ under different strain condition.

The effect of point-defect-driven flattening of polar phonon bands in doped fluorite MO_2 (M=Hf, Zr) is believed to increase the flat polar phonon bands and thus enlarge the possibility of polar modes and magnitude of dipole moment, leading to a stabilized o-phase and an enhanced ferroelectricity. We further studied the double-well energy landscape of the doped La$_x$M$_{1-x}$O$_2$. The energy barrier ΔE (eV/f.u.) first increases when x reaches to 12.5% and then decreases when x increases to 25% accompanied with a dramatically decreased P_S. The P_S of 12.5% La-doped HfO$_2$ slightly decreases from 70.0 μC·cm^-2 to 65.8 μC·cm^-2, while, the P_S increases from 64.7 μC·cm^-2 to104.5 μC·cm^-2 for 12.5% La-doped ZrO$_2$. For Vo-only doped case, the energy barrier obviously decreases at doping level of 12.5%. For example, the 12.5% V_O-doping at polar layer ($V_{O\text{-polar}}$) in HfO$_2$ system decreases the energy barrier from 1.345 eV to 1.007 eV whilst maintaining a high P_S even above 70.4 μC·cm^-2. The much lower energy barrier ΔE and higher P_S for $V_{O\text{-polar}}$-only doped case suggest a better ferroelectric performance compared with the case where V_O locates at the antipolar layer ($V_{O\text{-nonpolar}}$) as well as La-doped ones. However, both the more flattened polar phonon modes for La-doped HfO$_2$ with doping level in the range of 6.25%-12.5% and for V_O-only doped ZrO$_2$ is consistent with the generally higher ferroelectric performances experimentally observed in doped MO_2[6,14,36–44]. Since La-doped ZrO$_2$ shows similar enhanced flattened polar phonon bands, it is reasonable to predict high-performance ferroelectricity in 6.25–12.5% La-doped ZrO$_2$ and V_O-only doped ZrO$_2$.

The above results suggest a key role of V_O to achieve high-performance ferroelectricity in fluorite MO_2 compared with the La dopant. However, for the origin of the enhanced flattened bands in doped structure, we think there are three main reasons. First, there is no standard definition of flat phonon bands. We take the band with frequency difference $\Delta\omega$ between Γ to Y wave vectors

within 0.5 THz as flat phonon band, which is actually a kind of softening of the phonon bands and have been reported in defect-engineered materials[50–52]. Therefore, the doping-induced disorder would lead to the softening of phonon mode and flatten the phonon band, which enhances the flattening of the phonon bands. Second, in the doped cases, due to the local symmetry breaking, the lattice vibration mode becomes different from that in pure case. Especially the antipolar phonon band no longer conserves the antipolar state and results even in a net polarization. In this case, it may become even quite polar that can be evidenced by the local defect-dipolar states with net total polarization in each direction detailed in Fig. 5a. Finally, in La-doped structure, the longer bond-length of La-O (2.2–2.8 Å) than that of Zr–O (2–2.2 Å) would be able to decrease the elastic interaction between neighboring oxygen and cation around the point defect that is consistent with literature[4]. By taking 12.5% La-doped ZrO$_2$ as an example (Supplementary Figure 9), doping significantly decrease the spring interaction between neighboring ions around the point-defects. Therefore, more phonon bands become flat and polar due to the longer interaction between some host ions around the point defects. From a thermodynamic point of view, the energy difference between o-phase and m-phase decreases with La doped. The flattened bands reflect the stability of ferroelectric phase with La doping, and also imply that the o-phase is more accessible with La doping. As a whole, we think the point-defect-induced local symmetry breaking, stabilized o-phase, and the weaker interaction between the host ions around the point-defects would be responsible for the flattened phonon bands in the La-doped MO_2 (M = Zr, Hf).

Since both defects and epitaxial strain can affect the ferroelectricity, we also analyzed the effect of epitaxial strain on the phonon band structures. Fig. 4a, b show that there is no obvious variation in the distribution of the flat polar phonon band
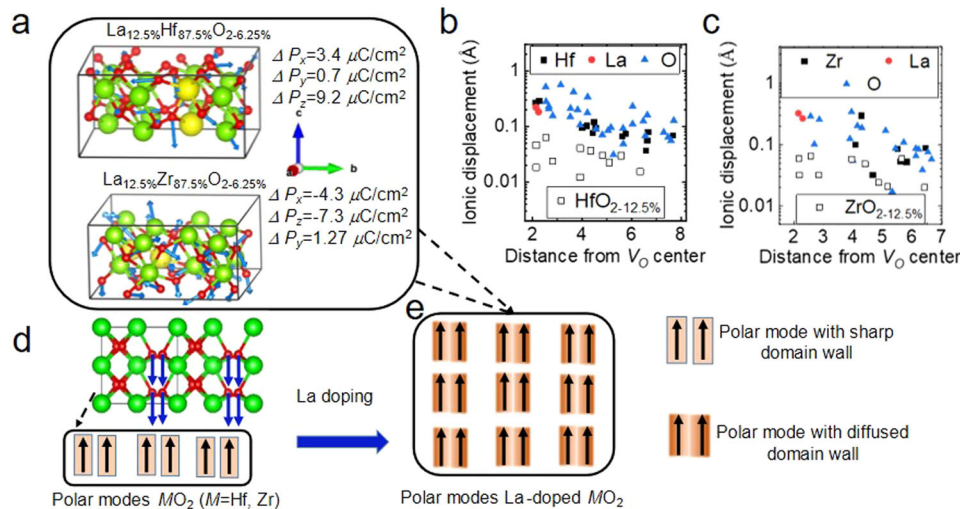
Fig. 5 Theoretical DFT calculation of local defect-dipolar states. a The local structures in 12.5% La-doped MO_2 ($M =$ Hf, Zr) around the La-V_O defect center show significant ionic relaxations with partially diffused domain walls, with both oxygen and M displacement relative to pure one. The pink and blue arrows reflect the ionic displacement within the crystal structures. **b, c** Ionic displacements of doped MO_2 relative to pure one as a function of radial distance from the V_O defect, indicating that the majority of ionic displacement occurs in the vicinity of La-V_O defect pairs, within 10 Å scope from the V_O. The result of V_O-only doped MO_2 where V_O at polar layer is provided as comparisons. **d** Schematic illustration of the polar modes with sharp domain walls in pure MO_2. **e** Schematic illustration of the normal polar modes with localized electric dipoles and sharp domain walls together with the point-defect induced polar modes with spread electric dipoles and diffused domain walls in La-doped MO_2. The red sphere and aqua green sphere indicate oxygen and host cation, respectively. The polar phonon bands were indicated in **d** and **e** relative to the sharpness of the domain walls. The red, green, and yellow spheres indicate oxygen, host cation, and La dopants, respectively.

frequencies ($\Delta\omega$) of ±4% uniaxially and biaxially strained o-HfO$_2$ in different directions (More details see Supplementary Figs. 10 and 11). Similar results were observed in strained o-ZrO$_2$ as shown in Fig. 4c, d. As we expected, the results under biaxial strains were basically consistent with the results under uniaxial strains. Above all, within 5% strain, the flatness of phonon band in o-phase is stable and robust. These results suggest that point-defect plays a more important role in the flattening of the polar phonon band and scale-free ferroelectricity. The dramatically enhanced flattened polar phonon bands suggest point-defects to be effective to engineer the ferroelectricity in fluorite-based ferroelectrics.

Defect-dipolar states in fluorite MO_2 ($M =$ Hf and Zr)
Point defects can induce local distortion due to mismatched size relative to host ions[18,29,53–55]. In conventional perovskite metal oxides, point-defect induced defect-dipoles and their correlation with intrinsic polarization are general due to the symmetry-conforming property of point defects[56]. Based on multi-scale simulations, we also reported that ferroelectric-like polarization hysteresis can be obtained in Mg-doped TiO$_2$ due to defect-driven local symmetry breaking[29]. In non-ferroelectric SrTiO$_3$, ferroelectric polarization behavior can also experimentally be observed to arise from nano-polar-regions associated with point defects[30,55]. Similar behavior of strap waist hysteresis loop in conventional perovskite ferroelectrics[20] has also been observed in ZrO$_2$[57], suggesting that the collective behavior of defect-dipoles also works in fluorite MO_2 (M=Hf, Zr). Therefore, it is necessary to figure out how the point defect interacts with the nearby environment or how the defect-dipoles affect the surrounding electric polarization.

As might be expected, M ($M =$ Hf, Zr) and oxygen ions especially the latter displaced three-dimensionally around the point defect. The lowest energy state was identified as the local structures illustrated in Fig. 5a for both systems. As shown in Fig. 5b, c, the magnitude of the ionic displacements relative to undoped o-MO_2 was obviously correlated with the distance from La-V_O defect complex, with the largest exceeding 0.6 Å and 1.0 Å by oxygen ion

in 12.5% La-doped HfO$_2$ and ZrO$_2$, respectively. The ionic displacement becomes more obvious in 25% La-doped MO_2 (Supplementary Fig. 12). While, V_O-only doped cases with V_O at polar layer (Fig. 5b-c) and antipolar layer (Supplementary Fig. 13) generally show much lower ionic displacement. This result suggests that defect-induced dipole is nucleated by the presence of La and its neighboring V_O which then drives surrounding oxygen to move-off-center with large displacement, resulting in a "super" dipole and large local lattice distortion. This process is similarly as that in Mg-doped TiO$_2$ where Mg-V_O defect cluster drive the local symmetry breaking to form a "super" dipole[29]. The large lattice distortion may provide an explanation for the generally higher polarization but higher energy barrier and coercive field compared with V_O-only doped cases.

For pure case, the zero-width sharp domain wall of the pure case originally comes from the condensation of polar and antipolar phonon bands in phase with equal magnitude to generate an orthorhombic structure that consists of alternating spacer layers and ferroelectric layers with up and down polarization respectively. Therefore, the generation of strict antipolar mode and its equal magnitude with polar mode would be two main pre-requisite conditions that are critical to induce the zero-domain walls. With La doping, local symmetry breaking emerges around the 'La-V_O-La' defect like that in Mg-doped TiO$_2$ that we previously reported[29], which is believed to break the two main pre-requisite conditions for zero-width domain walls. The point-defect dipoles polarize the surrounding Zr and oxygen ions to give rise to spread electric dipoles and distort the dead/ antipolar layer, in which case the antipolar modes are hard to conserve strict antipolar state and maintain the equal magnitude with polar mode. This is why the point-defect-induced local symmetry breaking areas show net total polarizations in x, y, and z directions (Fig. 5a).

Therefore, the point-defect induced lattice distortion greatly tuned the sharpness of domain walls. As shown in Fig. 5d, e, the polarization in pure o-MO_2 is mainly from flat polar phonon modes with localized electric dipoles and sharp domain walls. While in

doped cases, flat polar phonon modes give rise to generally diffused domain walls, which is responsible for the stabilized/ enhanced ferroelectricity in doped fluorite MO_2 ($M =$ Hf, Zr). The increased number of polar flat bands would be mainly related to the number of polar states or polarizability of the lattice. This is consistent with the recently reported reversible oxygen migration and phase transitions in hafnia-based ferroelectric devices where ferroelectricity is unmistakably intertwined with oxygen vacancy[49].

However, the much larger lattice distortion introduced by La-V_O pairs accompanied with much larger energy barrier compared with V_O-only doped case suggests that moderate local lattice distortion and concentration of V_O are vital for high-performance ferroelectricity. To further understand the scale-free ferroelectricity, we calculated the zero-energy domain wall (Supplementary Fig. 14). For pure HfO$_2$ and ZrO$_2$, the negative domain wall energy for the antiferroelectric $Pbca$ and ferroelectric $Pca2_1$ suggests that the antiferroelectric $Pbca$ is more stable. However, compared with the pure one, for HfO$_2$, 6.25% La doping and polar oxygen vacancies would both help to stabilize $Pca2_1$ phase. While, for ZrO$_2$, 12.5% La doping concentration is the best, but the $Pbca$ phase is still a more stable phase. Therefore, the scale-free ferroelectricity is still guaranteed in the doped cases. These results would inspire the understanding and exploration of the defect-induced ferroelectricity in similar fluorite MO_2-based thin films and other doping-induced ferroelectric systems, such as doped AlN, GaN, and ZnO where similarly MV level of coercive field is generally the case[6,7,58–63]. For memory devices, the application of fluorite MO_2 would be expected to further consider the effect of diffused and sharp domain walls on the ferroelectric stability of the memory devices.

In this work, we have confirmed instability modes in the phonon band of fluorite MO_2 ($M =$ Hf, Zr), leading to the transformation of c-phase to o-phase and t-phase. The appearance of o-phase is accompanied by flat polar phonon bands with extremely localized electric dipoles, which explains the scale-free ferroelectricity in fluorite MO_2 ultrathin film compared with the spread dipoles in conventional perovskite ferroelectrics. By analyzing La-doped MO_2 and V_O-only doped MO_2, all the doped cases show significantly flattened polar phonon bands. Their significantly enhanced flatness of polar phonon bands compared with of the pure ones, indicating an increased population of localized electric dipoles in the doped-MO_2. Moreover, there is no obvious polar phonon band in the non-flat ones, which means that the main contribution to the polarization is from flat polar phonon bands. The quasi-phonon-glass dynamics in doped MO_2 with significantly flattened phonon bands may suggest a giant anisotropic thermal rectification effect in the film and inspire further design in highly integrated circuits. There is no obvious variation in the flatness of polar phonon bands in epitaxially strained MO_2 compared with the La-doped ones, which suggests that the point defect plays a more vital role in the induced/ enhanced ferroelectricity in fluorite MO_2. Different from the localized electric dipoles with sharp zero-width domain walls in pure o-MO_2, the point-defect-induced local symmetry breaking in doped cases lead to collective electric polarization across the point-defect, which changes the very sharp zero-width domain walls with localized electric dipole observed in pure case into diffused domain walls with spread electric dipoles. The La-Vo defect pairs induce significantly higher local lattice distortion with significantly flattened polar phonon bands and generally higher energy barrier compared with V_O-only doped case, suggesting that a moderate local lattice distortion and V_O are vital for achieving high-performance ferroelectricity. Our results would advance the fundamentally understanding of the induced ferroelectricity in fluorite ferroelectrics. The defect-driven flattened polar phonon band may also inspire the investigation of the ferroelectric origin in doping-induced ferroelectric systems from the atomic-level, such as doped AlN, GaN, and ZnO.

METHODS
Computational methods

All calculations are carried out using the projector augmented-wave (PAW)[64] method as implemented in the Vienna Ab-initio Simulation Package (VASP)[65]. The Perdew–Burke–Ernzerhof (PBE)[66,67] functional under the generalized gradient approximation(GGA) is applied to deal with the exchange and correlation interactions. The Zr(4 s,4p,4d,5 s), La(5 s,5p,5d,6 s) and O(2 s, 2p) electron orbitals are treated as valence states with following atomic valence configurations: Zr($4s^24p^44d^25s^2$), La($5s^25p^65d^16s^2$), and O($2s^22p^6$). The cutoff energy of plane wave is set to be 600 eV which is large enough for energy convergency. To model the effect of concentration and figure out the defect states with lowest energy configuration, $1 \times 1 \times 1$, $2 \times 2 \times 1$, and $2 \times 2 \times 2$ supercells based on unperturbed rhombohedra MO_2 were constructed. The $7 \times 7 \times 7$ Monkhorst-Pack[68] k-points mesh is applied for the first Brillouin zone of the 12 atom unit cells and $3 \times 3 \times 3$ Monkhorst-Pack k-points grid for $2 \times 2 \times 2$ 96-atom supercells for pure and doped MO_2 for phonon spectra calculation. The force tolerance for the structure optimization and total energy were respectively converged to 10^{-2} eV Å^{-1} and 10^{-6} eV. The phonon dispersion was calculated by density functional perturbation theory (DFPT) using Phonopy[69,70]. The energy barrier for the polarization switching was calculated by the nudged elastic band method (NEB) and the result is consistent with the double-well potential based on Landau-Ginzburg-Devonshire (LGD) theory. Berry phase calculations were performed to calculate the spontaneous polarization on o-phase cells. The polarization quantum has been taken into consideration for data correction.

DATA AVAILABILITY
The data that support the findings of this study are available from the corresponding author upon reasonable request.

REFERENCES
1. Li, S. et al. Ferroelectric thin films: performance modulation and application. *Mater. Adv.* **3**, 5735–5752 (2022).
2. Setter, N. & Damjanovic, D. Ferroelectric thin films Review of materials, properties, and applications. *J. Appl. Phys.* **100**, 051606 (2005).
3. Junquera, J. & Ghosez, P. Critical thickness for ferroelectricity in perovskite ultrathin films. *Nature* **422**, 506–509 (2003).
4. Lee, H.-J. et al. Scale-free ferroelectricity induced by flat phonon bands in HfO$_2$. *Science* **369**, 1343–1347 (2020).
5. Cheema, S. S. et al. Emergent ferroelectricity in subnanometer binary oxide films on silicon. *Science* **376**, 648–652 (2022).
6. Muller, J. et al. Ferroelectricity in Simple Binary ZrO$_2$ and HfO$_2$. *Nano Lett.* **12**, 4318–4323 (2012).
7. Materlik, R., Künneth, C. & Kersch, A. The origin of ferroelectricity in Hf$_{1-x}$Zr$_x$O$_2$ A computational investigation and a surface energy model. *J. Appl. Phys.* **117**, 134109 (2015).
8. Kisi, E. H., Howard, C. J. & Hill, R. J. Crystal structure of orthorhombic zirconia in partially stabilized zirconia. *J. Am. Ceram. Soc.* **72**, 1757–1760 (1989).
9. Yurchuk, E. et al. Impact of layer thickness on the ferroelectric behaviour of silicon doped hafnium oxide thin films. *Thin Solid Films* **533**, 88–92 (2013).
10. Xu, X. et al. Kinetically stabilized ferroelectricity in bulk single-crystalline HfO$_2$:Y. *Nat. Mater.* **20**, 826–832 (2021).
11. Wei, Y. et al. A rhombohedral ferroelectric phase in epitaxially strained Hf$_{0.5}$Zr$_{0.5}$O$_2$ thin films. *Nat. Mater.* **17**, 1095–1100 (2018).
12. Chen, H. et al. Obvious ferroelectricity in undoped HfO$_2$ films by chemical solution deposition. *J. Mater. Chem. C* **8**, 2820–2826 (2020).
13. Tabata, T., Halty, S., Rozé, F., Huet, K. & Mazzamuto, F. Non-doped HfO$_2$ crystallization controlled by dwell time in laser annealing. *Appl. Phys. Express* **14**, 115503 (2021).

14. Yun, Y. et al. Intrinsic ferroelectricity in Y-doped HfO₂ thin films. *Nat. Mater.* **21**, 903–909 (2022).

15. Chernikova, A. G. et al. Improved ferroelectric switching endurance of La-doped Hf0.5Zr0.5O2 thin films. *ACS Appl. Mater. Interfaces* **10**, 2701–2708 (2018).

16. Schroeder, U. et al. Impact of different dopants on the switching properties of ferroelectric hafniumoxide. *Jpn J. Appl. Phys.* **53**, 08LE02 (2014).

17. Liu, S. & Hanrahan, B. M. Effects of growth orientations and epitaxial strains on phase stability of HfO₂ thin films. *Phys. Rev. Mater.* **3**, 054404 (2019).

18. Chouprik, A., Negrov, D., Tsymbal, E. Y. & Zenkevich, A. Defects in ferroelectric HfO₂. *Nanoscale* **13**, 11635–11678 (2021).

19. Eichel, R.-A. et al. Defect-dipole formation in copper-doped PbTiO₃ ferroelectrics. *Phys. Rev. Lett.* **100**, 095504 (2008).

20. Lee, D. et al. Active control of ferroelectric switching using defect-dipole engineering. *Adv. Mater.* **24**, 6490–6495 (2012).

21. Zhao, B. et al. Ferroelectric polarization and defect-dipole switching in an epitaxial (111) BiFeO₃ thin film. *J. Appl. Phys.* **117**, 204103 (2015).

22. Damodaran, A. R., Breckenfeld, E., Chen, Z., Lee, S. & Martin, L. W. Enhancement of ferroelectric curie temperature in BaTiO₃ films via strain-induced defect dipole alignment. *Adv. Mater.* **26**, 6341–6347 (2014).

23. Li, F. et al. Giant piezoelectricity of Sm-doped Pb(Mg₁/₃Nb₂/₃)O₃-PbTiO₃ single crystals. *Science* **364**, 264–268 (2019).

24. Li, F. et al. Ultrahigh piezoelectricity in ferroelectric ceramics by design. *Nat. Mater.* **17**, 349–354 (2018).

25. Xiao, H. et al. Design for highly piezoelectric and visible/near-infrared photoresponsive perovskite oxides. *Adv. Mater.* **31**, 1805802 (2019).

26. Hu, W. et al. Electron-pinned defect-dipoles for high-performance colossal permittivity materials. *Nat. Mater.* **12**, 821–826 (2013).

27. Dong, W. et al. Colossal dielectric behavior of Ga+Nb co-doped rutile TiO₂. *ACS Appl. Mater. Interfaces* **7**, 25321–25325 (2015).

28. Dong, W. et al. Colossal permittivity with ultralow dielectric loss in In + Ta co-doped rutile TiO₂. *J. Mater. Chem. A* **5**, 5436–5441 (2017).

29. Dong, W. et al. Collective nonlinear electric polarization via defect-driven local symmetry breaking. *Mater. Horiz.* **6**, 1717–1725 (2019).

30. Lee, D. et al. Emergence of room-temperature ferroelectricity at reduced dimensions. *Science* **349**, 1314–1317 (2015).

31. Lee, D. H., Lee, Y., Yang, K. & Park, J. Y. Domains and domain dynamics in fluoritestructured ferroelectrics. *Appl. Phys. Rev.* **8**, 021312 (2021).

32. Wang, J., Li, H. P. & Stevens, R. Hafnia and hafnia-toughened ceramics. *J. Mater. Sci.* **27**, 5397–5430 (1992).

33. Leger, J. M., Tomaszewski, P. E., Atouf, A. & Pereira, A. S. Pressure-induced structural phase transitions in zirconia under high pressure. *Phys. Rev. B. Condens. Matter* **47**, 14075–14083 (1993).

34. Al-Khatatbeh, Y., Lee, K. K. M. & Kiefer, B. Phase relations and hardness trends of ZrO₂ phases at high pressure. *Phys. Rev. B* **81**, 214102 (2010).

35. Barabash, S. V., Pramanik, D., Zhai, Y., Magyari-Kope, B. & Nishi, Y. Ferroelectric Switching pathways and energetics in (Hf,Zr)O₂. *ECS Trans.* **75**, 107–121 (2017).

36. Böscke, T. S., Müller, J., Bräuhaus, D., Schröder, U. & Böttger, U. *Ferroelectricity in Hafnium Oxide: CMOS Compatible Ferroelectric Field Effect Transistors. IEEE Int. Electron Devices Meet 24.5.1–24.5.4* (IEEE, 2011).

37. Lin, B.-T., Lu, Y.-W., Shieh, J. & Chen, M.-J. Induction of ferroelectricity in nanoscale ZrO₂ thin films on Pt electrode without post-annealing. *J. Eur. Ceram. Soc.* **37**, 1135–1139 (2017).

38. Mueller, S. et al. Ferroelectricity in Gd-Doped HfO₂ Thin Films. *ECS J. Solid. State Sci. Technol.* **1**, N123–N126 (2012).

39. Mueller, S. et al. Incipient ferroelectricity in Al-doped HfO₂ thin films. *Adv. Funct. Mater.* **22**, 2412–2417 (2012).

40. Müller, J. et al. Ferroelectricity in yttrium-doped hafnium oxide. *J. Appl. Phys.* **110**, 114113 (2011).

41. Schenk, T. et al. *Strontium Doped Hafnium Oxide Thin Films: Wide Process Window For Ferroelectric Memories* (IEEE, 2013).

42. Starschich, S., Schenk, T., Schroeder, U. & Boettger, U. Ferroelectric and piezoelectric properties of Hf₁₋ₓZrₓO₂ and pure ZrO₂ films. *Appl. Phys. Lett.* **110**, 182905 (2017).

43. Wang, J. et al. Ferroelectric properties of pure ZrO₂ thin films by chemical solution deposition. *Ceram. Int.* **47**, 16845–16851 (2021).

44. Zou, Z. et al. Enhancement of ferroelectricity and homogeneity of orthorhombic phase in Hf0.5Zr0.5O2thin films. *Nanotechnology* **32**, 335704 (2021).

45. Shibayama, S., Nagano, J., Sakashita, M. & Nakatsuka, O. Ferroelectric phase formation for undoped ZrO₂ thin films by wet O₂ annealing. *Jpn J. Appl. Phys.* **59**, SMMA04 (2020).

46. Yang, Z. et al. Flat phonon modes driven ultralow thermal conductivities in Sr₃AlSb₃ and Ba₃AlSb₃ Zintl compounds. *Appl. Phys. Lett.* **120**, 142103 (2022).

47. Zhang, Y. et al. Simultaneous electrical and thermal rectification in a monolayer lateral heterojunction. *Science* **378**, 169–175 (2022).

48. Miyata, K. & Zhu, X. Y. Ferroelectric large polarons. *Nat. Mater.* **17**, 379–381 (2018).

49. Nukala, P. et al. Reversible oxygen migration and phase transitions in hafnia-based ferroelectric devices. *Science* **372**, 630–635 (2021).

50. Sirenko, A. A. et al. Soft-mode hardening in SrTiO₃ thin films. *Nature* **404**, 373–376 (2000).

51. Sirenko, A. A. et al. Observation of the first-order raman scattering in SrTiO₃ films. *Phys. Rev. Lett.* **82**, 4500–4503 (1999).

52. Singh, F., Singh, R. G., Kumar, V., Khan, S. A. & Pivin, J. C. Softening of phonons by lattice defects and structural strain in heavy ion irradiated nanocrystalline zinc oxide films. *J. Appl. Phys.* **110**, 083520 (2011).

53. Dong, W. et al. Engineering the defects and microstructures in ferroelectrics for enhanced/novel properties: an emerging way to cope with energy crisis and environmental pollution. *Adv. Sci.* **9**, 2105368 (2022).

54. Schroeder, U., Park, M. H., Mikolajick, T. & Hwang, C. S. The fundamentals and applications of ferroelectric HfO₂. *Nat. Rev. Mater.* **7**, 653–669 (2022).

55. Feng, Y. et al. Defects and aliovalent doping engineering in electroceramics. *Chem. Rev.* **120**, 1710–1787 (2020).

56. Ren, X. Large electric-field-induced strain in ferroelectric crystals by point-defect-mediated reversible domain switching. *Nat. Mater.* **3**, 91–94 (2004).

57. Starschich, S. & Böttger, U. Doped ZrO₂ for future lead free piezoelectric devices. *J. Appl. Phys.* **123**, 044101 (2018).

58. Tasnadi, F. et al. Origin of the anomalous piezoelectric response in wurtzite Sc(x)Al(1-x)N alloys. *Phys. Rev. Lett.* **104**, 137601 (2010).

59. Wolff, N., Fichtner, S. & Haas, B. Atomic scale confirmation of ferroelectric polarization inversion in wurtzite-type AlScN. *J. Appl. Phys.* **129**, 034103 (2020).

60. Fichtner, S., Wolff, N., Lofink, F., Kienle, L. & Wagner, B. AlScN: A III-V semiconductor based ferroelectric. *J. Appl. Phys.* **125**, 114103 (2018).

61. Zhu, W. et al. Strongly temperature dependent ferroelectric switching in AlN, Al₁₋ₓScₓN, and Al₁₋ₓBₓN thin films. *Appl. Phys. Lett.* **119**, 062901 (2021).

62. Wang, D., Wang, P., Wang, B. & Mia, Z. Fully epitaxial ferroelectric ScGaN grown on GaN by molecular beam epitaxy. *Appl. Phys. Lett.* **119**, 111902 (2021).

63. Ferri, K., Bachu, S. & Zhu, W. Ferroelectrics everywhere: ferroelectricity in magnesium substituted zinc oxide thin films. *J. Appl. Phys.* **130**, 044101 (2021).

64. Kresse, G. & Joubert, D. From ultrasoft pseudopotentials to the projector augmented-wave method. *Phys. Rev. B* **59**, 1758 (1998).

65. Kresse, G. & Furthmiiller, J. Efficiency of ab-initio total energy calculations for metals and semiconductors using a plane-wave basis set. *Comp. Mater. Sci.* **6**, 15–50 (1996).

66. Vanderbilt, D. Soft self-consistent pseudopotentials in a generalized eigenvalue formalism. *Phys. Rev. B. Condens. Matter* **41**, 7892–7895 (1990).

67. Perdew, J. P., Burke, K. & Ernzerhof, M. Generalized gradient approximation made simple. *Phys. Rev. Lett.* **77**, 3865 (1996).

68. Chadi, D. J. Special points for Brillouin-zone integrations. *Phys. Rev. B* **16**, 1748–1749 (1977).

69. Gonze, X. & Lee, C. Dynamical matrices, Born effective charges, dielectric permittivity tensors, and interatomic force constants from density-functional perturbation theory. *Phys. Rev. B* **55**, 10355 (1997).

70. Giannozzi, P., de Gironcoli, S., Pavone, P. & Baroni, S. Ab initio calculation of phonon dispersions in semiconductors. *Phys. Rev. B* **43**, 7231–7242 (1991).

ACKNOWLEDGEMENTS

AUTHOR CONTRIBUTIONS

W.D. and Q.F. initiated the project. P.A. and F.Y. run the calculation with the assistance from K.X., S.L., J.Z., Q.M., S.H.B., Y.L., and M.H.; W.D. and Q.F. analyzed the data with the assistance from X.H., L.Y., G.Z., W.L., and S.J.; P.A., F.Y., and W.D. wrote the manuscript. All the authors revised and polished the manuscript.

COMPETING INTERESTS

The authors declare no competing interests.

ADDITIONAL INFORMATION